Accretionary Pedogenesis and Holocene Climate Evolution in Black Soil Region of Northeast China: Evidence from a Sedimentary Profile

Yangyang Chen [a, b, c], Ke Yang [a, c, d, *], Fubing He [e], Junbo Yu [a, c], Zhiwei Yang [a, c], Shaozhong Qiao [a, c], Jiayu Wang [a, c], Xinyi Wang [a, c], Jiacheng Liu [a, c], Xue Liu [a, c], Chenchen Wang [a, c]

[a] Harbin Natural Resources Survey, China Geological Survey, Harbin 150086, China

[b] Northeast Geological S&T Innovation Center of China Geological Survey, Shenyang 110034, China

[c] Observation and Research Station of Earth Critical Zone in Black Soil, Harbin, Ministry of Natural Resources 150086, China

[d] Institute of Geophysical and Geochemical Exploration, Chinese Academy of Geological Sciences, Langfang 065000, China

[e] Beijing Institute of Geological Survey, Beijing 102206, China

Abstract: The black soil region of the Songnen Plain, one of the world's three major black soil belts, is critical for China's grain security, yet the formation mechanism of its thick, organic-rich soils remains insufficiently quantified. In this study, we investigate the ZYHPM01 profile in the eastern Songnen Plain using grain-size end-member analysis (EMA), multi-proxy geochemical tracers, and coarse-grained quartz optically stimulated luminescence (OSL) dating. The EMA identifies three sedimentary components: EM1 represents distal background dust transported via high-altitude suspension; EM2 and EM3 indicate proximal dust inputs driven by the winter monsoon. Based on the OSL-based chronostratigraphy constructed using piecewise linear regression, the Holocene evolution is divided into five stages. Following rapid accumulation in the Early Holocene (11.63 – 10.31 ka BP), the region experienced a climatic setback during the transition to the Middle Holocene, broadly consistent with high-latitude cooling episodes such as the 8.2 ka event. The Mid-Holocene Climatic Optimum (6.72 – 5.11 ka BP) established a warm-humid environment, with peak CIA values (~68.8) and minimum Sr/Cu ratios (~7.0) confirming intense chemical weathering and leaching, which served as the primary environmental window for black soil initiation. This period was terminated by an abrupt shift to cold-dry conditions in the Late Holocene, characterized by enhanced coarse-grained dust inputs driven by a strengthened winter monsoon. We propose a Formation-Preservation mechanism: the Mid-Holocene provided optimal hydrothermal conditions for intense chemical weathering, high biological productivity, and active pedogenesis (Formation Phase), while the subsequent Late Holocene climatic deterioration inhibited microbial decomposition and restricted chemical leaching, effectively preserving the accumulated organic carbon (Preservation Phase). These findings reveal that modern black soil in the Songnen Plain is a legacy of peak Mid-Holocene productivity preserved by climatic cooling, providing new insights for understanding critical zone evolution at monsoon margins.

Keywords: Songnen Plain; end-member analysis; OSL dating; Accretionary pedogenesis; black soil formation; Holocene climate evolution

1. Introduction

The black soil region of the eastern Songnen Plain serves as a critical "ballast stone" for China's grain security and is a vital component of the global food system (Han and Li, 2018; Tong et al., 2024). While renowned for its deep humus layer and exceptional fertility, this resource faces severe degradation under anthropogenic pressure (Liu et al., 2025; Qiu et al., 2022; Xu et al., 2025; Zhang et al., 2015). To implement sustainable conservation strategies, it is imperative to understand its natural formation limits. Unlike soils developed on stable bedrock, the black soil in this region is a product of "Accretionary Pedogenesis"—a dynamic process where soil formation occurs simultaneously with the continuous deposition of aeolian dust (Yang et al., 2023; Zhang et al., 2024a). This implies that the genesis of black soil is recorded not only in its chemical weathering signatures but also in the physical dynamics of sediment accumulation driven by the East Asian Monsoon.

Existing studies have established a foundational understanding of the timing and provenance of black soil in the Songnen Plain. The initiation of black soil development is generally traced to the early-to-mid Holocene, occurring no later than 8.5 ka BP (Cui et al., 2021; Zhang et al., 2023). Regarding the parent material, a consensus has emerged on its multi-source origin, encompassing distal aeolian loess (Shi et al., 2024; Wu et al., 2022), alluvial deposits, and in situ residual materials (Han and Li, 2018). Among these, aeolian sediments are identified as a key component. Research indicates that these materials are derived from a complex mix of long-distance input from upwind arid regions (e.g., Gobi Desert, Mongolian Plateau) and proximal contributions from regional sandy lands such as the Horqin and Songnen fields (Li et al., 2025; Sun, 2002; Xie et al., 2019; Zhang et al., 2024b; Zhao et al., 2007). Furthermore, fluctuations in the East Asian Monsoon and Westerlies since the Holocene have been identified as the primary drivers controlling these wind regimes, dust transport pathways, and vegetation dynamics (Dallmeyer et al., 2013; Wu et al., 2023).

Despite this progress, reconstructing the precise evolutionary history of black soil remains challenged due to methodological bottlenecks. First, disentangling the complex signals of aeolian deposition and pedogenic processes requires integrated multi-proxy approaches. While geochemical proxies (e.g., CIA, Rb/Sr) are widely used indicators of chemical weathering intensity, their interpretation in dynamic aeolian environments requires careful consideration of sediment source variations and post-depositional processes. Second, establishing a robust chronology is difficult due to intense pedoturbation. In black soils, biological mixing often compromises bulk organic dating and fine-grained luminescence dating (Cheng et al., 2018). Consequently, the specific mechanisms driving the interplay between sediment accumulation rates and organic matter preservation remain insufficiently quantified.

This study focuses on the ZYHPM01 profile in the eastern Songnen Plain using an integrated approach to address these issues. We employed Grain Size End-Member Analysis (EMA) (Dietze et al., 2012; Niu et al., 2024; Weltje and Prins, 2003) to quantitatively identify distal versus proximal

sedimentary components. Crucially, we utilized coarse-grained quartz (125 – 180 μm) for optically stimulated luminescence (OSL) dating to minimize the effects of post-depositional mixing associated with finer fractions. Furthermore, by coupling these methods with multi-proxy geochemical analysis, this study aims to: (1) reconstruct the Holocene sedimentary and climatic history in the eastern Songnen Plain; (2) characterize the relationship between aeolian deposition dynamics and chemical weathering intensity; and (3) propose a formation model that links climate-modulated sedimentary dynamics to the formation and preservation of black soil resources. The research findings not only deepen scientific understanding of the genesis of black soil in the Songnen Plain and its response to climate change but also provide theoretical support for the sustainable management strategies of regional black soil resources.

2. Materials and methods

2.1. Study region

The Songnen Plain (Fig. 1a) is located in the northeastern region of China, bordered by the Greater Khingan Mountains to the west, the Lesser Khingan Mountains to the north, the Changbai Mountains to the east, and the Liaohe Plain to the south. The terrain slopes gently from the higher elevations in the north to the lower elevations in the south, transitioning from peripheral mountainous areas to a central plain, with a roughly diamond-shaped planform (Chen et al., 2024; Hou et al., 2023). This plain was formed on the tectonic foundation of the Mesozoic Songliao Basin, shaped by a combination of geological processes, including aeolian activity, fluvial action, and lacustrine deposition, since the Quaternary (Fig. 1). The surface layer is characterized by thick accumulations of loosely consolidated Quaternary sediments (Xie et al., 2019). The study area has a temperate continental monsoon climate with distinct seasons and synchronized rainfall and heat. Annual precipitation varies significantly, with cold and prolonged winters and dry, windy springs, providing climatic conditions conducive to both aeolian activity and the development of black soil (Song et al., 2022).

The ZYHPM01 profile is located on a gently sloping terrace approximately 1.3 km northeast of Dongqijiatun, Zhayinhe Township, Hailun City (126.979304 ° E, 47.707992 ° N; elevation ~218.0 m). This area (Fig. 1) lies in the eastern Songnen Plain, within the undulating black soil region characterized by gently rolling hills, which represents a typical concentrated distribution zone of black soil (Shi et al., 2024). The modern surface vegetation around the profile is primarily cropland, with low natural vegetation coverage. The profile is situated on a relatively stable terrace crest with a northeastward orientation of 50° and reveals a depth of 1.6 m (Fig. 2).

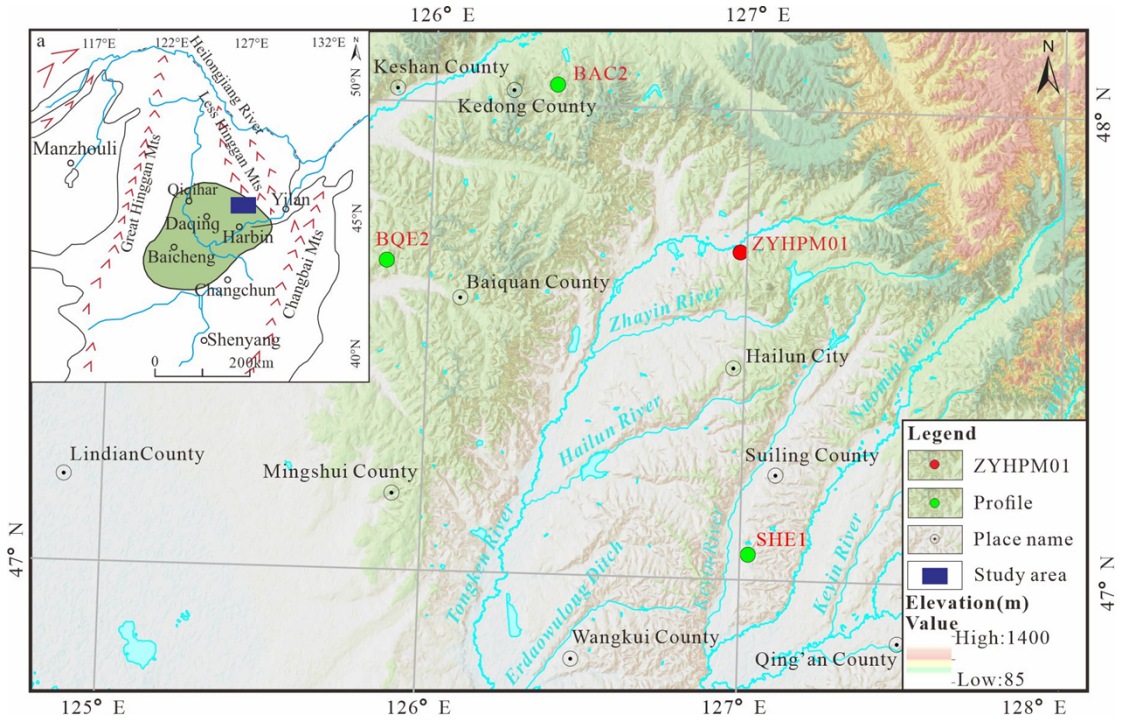

Fig. 1. The topographic map and the distribution of the profile position in the study area, and the schematic diagram of the Songnen Plain, Northeast China.

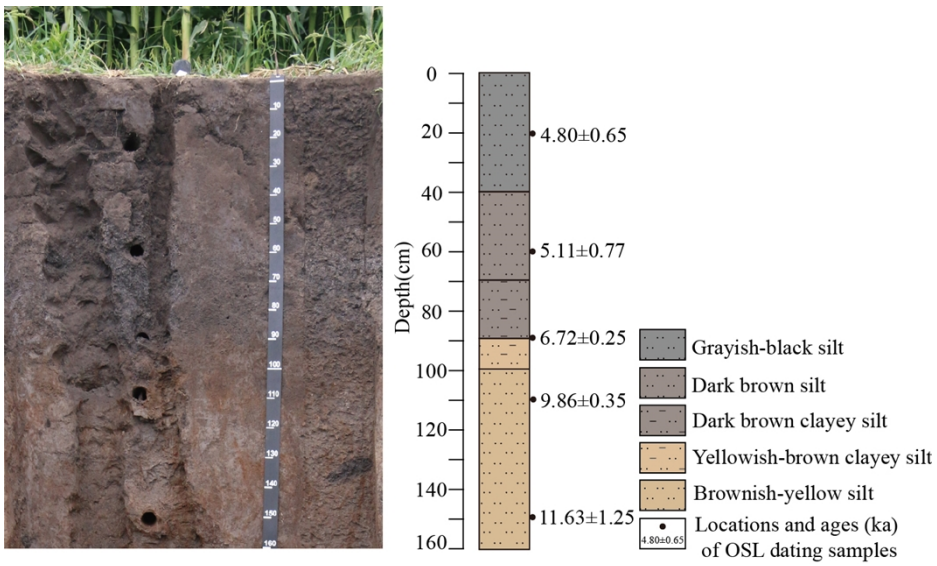

Fig. 2. The photographs and sketch map of ZYHPM01 profile, showing lithological layers and OSL sampling locations.

2.2. OSL dating

After cleaning the profile, five OSL dating samples were collected at depths of 0.2 m, 0.6 m, 0.9 m, 1.1 m, and 1.5 m (Fig. 2). The sampling process was conducted under light-restricted conditions. Stainless steel tubes with a diameter of approximately 5 cm and a length of 20 cm, with one end wrapped in a black plastic bag, were vertically inserted into the freshly exposed profile to collect undisturbed sediment samples. Each sample weighed approximately 500 g, and both ends of

the tubes were sealed with light-blocking materials and wrapped with black tape to prevent light exposure and moisture loss.

The pretreatment and measurement of OSL samples were conducted in the Luminescence Dating Laboratory at Jilin University. Sample pretreatment was performed in a darkroom under weak red-light conditions. Carbonates and organic matter were removed using 10% HCl and 30% H_2O_2, respectively. Unlike studies relying on fine silt, coarse-grained quartz (125 – 180 μm) were extracted to minimize the potential effects of post-depositional translocation associated with finer fractions. The coarse fraction was etched with 40% hydrofluoric acid (HF) for 40 minutes to remove the alpha-irradiated outer layer and eliminate feldspar contamination, followed by rinsing with HCl. The purity of the quartz extracts was confirmed by infrared stimulation (IR test). The equivalent dose (De) was determined using the single-aliquot regenerative dose (SAR) protocol (Murray and Wintle, 2000) on an automated Risø TL/OSL-DA-20 reader, with blue LED excitation light (470±30 nm) and a Hoya U-340 filter as the detection window. The preheat temperature for the quartz samples was set to 220 ℃ for 10 s, and measurements were conducted at 125 ℃. The environmental dose rate (Dr) was calculated based on the concentrations of U, Th, and K, which were measured using ICP-MS/ICP-OES techniques. The cosmic dose rate was estimated using the method (Prescott et al., 1994), considering sample burial depth, altitude, and geographic location. The final age calculations were performed using the formula (Aitken and Smith, 1988). To address potential partial bleaching or pedoturbation, the statistical analysis of De distributions was rigorously applied (details in Section 3.2).

2.3. Grain size measurement

For grain size analysis, 16 sediment samples were continuously collected at 0.1 m intervals from bottom to top along the profile (Fig. 2). In the laboratory, each sample was air-dried, and approximately 0.5 g was taken for pretreatment. Organic matter was removed using a 10% H_2O_2 solution, and carbonates were dissolved with 10% HCl solution. After the complete reaction, the samples were repeatedly centrifuged and rinsed with deionized water until a neutral pH was achieved. Subsequently, a 0.05 mol/L $(NaPO_3)_6$ solution was added as a dispersing agent, and the mixture was sonicated for 10 minutes to ensure complete particle dispersion.

Grain size analysis was performed at the Institute of Geophysical and Geochemical Exploration, Chinese Academy of Geological Sciences, using a Mastersizer 2000 laser particle size analyzer (Malvern Instruments, UK), with a measurement range of 0.01 – 2000 μm and a repeatability error of less than 1%. To ensure data reliability, 5% of the samples were randomly selected for duplicate testing, which demonstrated excellent consistency. Grain size fractions were classified according to the Udden-Wentworth logarithmic scale as follows: clay (<4 μm), fine silt (4 – 16 μm), medium silt (16 – 32 μm), coarse silt (32 – 63 μm), and sand (>63 μm). Grain size parameters, including median grain size (M_d), sorting coefficient (σ), skewness (SK), and kurtosis (KG), were calculated

following the formula (Folk and Ward, 1957).

2.4. Chemical analysis

A total of 16 samples, corresponding to the grain-size sampling horizons, were selected for elemental analysis at the Harbin Natural Resources Survey. All samples were oven-dried at 45 ℃ to a constant weight and ground to below 200 mesh using an agate mortar for further testing. Major element concentrations were determined by X-ray fluorescence spectroscopy (XRF, PANalytical Axios Max, Netherlands). Trace elements and rare earth elements (REE) concentrations were analyzed by inductively coupled plasma mass spectrometer (ICP-MS, Thermo Fisher Scientific Xseries 2) after sample digestion with a mixed acid solution (HF-HNO_3-$HClO_4$) under high pressure. Total organic carbon (TOC) was determined by the volumetric method after oxidation with a potassium dichromate-sulfuric acid solution ($K_2Cr_2O_7$-H_2SO_4) under external heating. Quality assurance and quality control (QA/QC) were ensured with certified reference materials (GSS series) and duplicate sample analyses. The analytical methods and their corresponding detection limits are detailed in Table 1. To ensure compliance with the precision and accuracy standards outlined for the GSS series, a random subset comprising 5% of the total samples was selected for parallel analysis during the testing phase. The duplicate sample evaluation revealed a 100% pass rate, confirming that the data quality fully satisfied the prescribed criteria. Detailed analysis of quality control methods can be found in Li et al. (2014).

Table 1

Laboratory analytical methods and detection limits.

Element	Unit	Analytical Methods	Detection Limit	Digestion Method
SiO_2	%	XRF	0.095	Pressed powder pellets
Al_2O_3	%	XRF	0.045	Pressed powder pellets
TFe_2O_3	%	XRF	0.049	Pressed powder pellets
MgO	%	XRF	0.02	Pressed powder pellets
CaO	%	XRF	0.046	Pressed powder pellets
Na_2O	%	XRF	0.03	Pressed powder pellets
K_2O	%	XRF	0.01	Pressed powder pellets
Ba	mg/kg	ICP-MS	8.53	$HF + HCl + HNO_3 + HClO_4$
Cu	mg/kg	ICP-OES	0.85	$HF + HCl + HNO_3 + HClO_4$
Rb	mg/kg	XRF	8	Pressed powder pellets
Sc	mg/kg	ICP-OES	0.7	$HF + HCl + HNO_3 + HClO_4$
Sr	mg/kg	ICP-MS	1.47	$HF + HCl + HNO_3 + HClO_4$
Th	mg/kg	ICP-MS	0.07	$HF + HCl + HNO_3 + HClO_4$
La	mg/kg	ICP-MS	1.13	$HF + HCl + HNO_3 + HClO_4$
Ce	mg/kg	ICP-MS	0.7	$HF + HCl + HNO_3 + HClO_4$
Pr	mg/kg	ICP-MS	0.01	$HF + HCl + HNO_3 + HClO_4$
Nd	mg/kg	ICP-MS	0.05	$HF + HCl + HNO_3 + HClO_4$
Sm	mg/kg	ICP-MS	0.02	$HF + HCl + HNO_3 + HClO_4$
Eu	mg/kg	ICP-MS	0.01	$HF + HCl + HNO_3 + HClO_4$
Gd	mg/kg	ICP-MS	0.05	$HF + HCl + HNO_3 + HClO_4$
Tb	mg/kg	ICP-MS	0.03	$HF + HCl + HNO_3 + HClO_4$
Dy	mg/kg	ICP-MS	0.02	$HF + HCl + HNO_3 + HClO_4$
Ho	mg/kg	ICP-MS	0.03	$HF + HCl + HNO_3 + HClO_4$
Er	mg/kg	ICP-MS	0.01	$HF + HCl + HNO_3 + HClO_4$
Tm	mg/kg	ICP-MS	0.03	$HF + HCl + HNO_3 + HClO_4$
Yb	mg/kg	ICP-MS	0.01	$HF + HCl + HNO_3 + HClO_4$
Lu	mg/kg	ICP-MS	0.02	$HF + HCl + HNO_3 + HClO_4$
TOC	%	Vol	0.1	$K_2Cr_2O_7$-H_2SO_4

2.5. Grain size EMA

A nonparametric endpoint model analysis was performed on the raw data of all 16 samples across 100 grain size channels. This analysis was conducted in the MATLAB (R2023a) environment utilizing the AnalySize software package (v. 1.2.2) (Paterson and Heslop, 2015). The method is based on the theoretical framework (Prins et al., 1999; Weltje, 1997), employing non-negative least squares and linear programming algorithms to decompose the grain size dataset into several EMs with fixed grain size distribution characteristics and their relative contributions in each sample. The choice of a three-end-member model was determined to provide the highest coefficient of determination ($R^2 > 0.95$) while ensuring each end member was geologically meaningful. Models with fewer end members failed to capture the full variability, while those with more introduced statistical noise without improving the geological interpretation. Pedoturbation can potentially mix sediment and thus blur the distinct signatures of the end members; however, the systematic and coherent stratigraphic variations of the EM components suggest that the primary depositional signals are largely preserved.

2.6. CIA calculation

To evaluate the intensity of chemical weathering in the source area, the CIA was calculated based on major element data. The formula is:

$$CIA = [Al_2O_3/(Al_2O_3 + CaO^* + Na_2O + K_2O)] \times 100 \quad (1)$$

where CaO* represents the CaO content derived from silicate minerals (Nesbitt and Young, 1982).

3. Results

3.1. Lithology characteristics

The lithology of the ZYHPM01 profile can be divided into five layers from top to bottom:

(1) Layer 0 – 0.2 m: cultivated layer, black-brown to dark gray-black silt with a loose texture, rich in organic matter and plant roots.

(2) Layer 0.2 – 0.6 m: black soil layer, blackish-brown sandy silt with a well-developed granular or blocky structure, homogeneous texture, and containing a small amount of plant roots.

(3) Layer 0.6 – 0.9 m: black soil layer, blackish-brown clayey silt, with well-developed granular or blocky structure, homogeneous texture, rich in humus. Occasional plant fragments are visible.

(4) Layer 0.9 – 1.2 m: yellowish-brown clayey silt, relatively homogeneous texture, with a small number of rust-yellow mottles and iron-manganese nodules.

(5) Layer 1.2 – 1.6 m: yellowish-brown silt, slightly coarse texture, with localized lenses of fine sand or silt-like clumps, and a small number of calcareous nodules or pseudo mycelium visible

in the lower part.

3.2. Chronology and sedimentation rate

The chronological framework for the ZYHPM01 profile was established using five OSL samples (Table 2). Analysis of equivalent dose (De) distributions reveals distinct optical characteristics across the profile. Samples collected from depths of 0.2 m, 0.9 m, and 1.1 m exhibit concentrated De distributions with low overdispersion (OD) values , indicating the sediments were well-bleached before deposition. Accordingly, the Central Age Model (CAM) was applied to these samples. Conversely, samples from 0.6 m and 1.5 m display broader, multi-modal dose distributions with higher OD values. For these datasets, the Finite Mixture Model (FMM) was employed to isolate the primary dose component and minimize the influence of post-depositional mixing. The resulting ages range from 4.80 ± 0.65 ka to 11.63 ± 1.25 ka and follow a consistent stratigraphic order with no reversals (Fig. 3).

The age-depth model constructed using piecewise linear regression reveals significant variations in sedimentation rate throughout the Holocene, with an overall average of approximately 12.9 cm/ka. Based on the age-depth relationship and sedimentological characteristics, the sedimentation history can be divided into five distinct stages. The profile begins with a high sedimentation rate of 22.73 cm/ka during the Early Holocene (1.6 m~1.2 m, 11.63 – 10.31 ka BP). Subsequently, sedimentation slows markedly to ~8.36 cm/ka between 10.31 and 6.72 ka BP (1.2 m~0.9 m). A rebound in accumulation occurs, with rates increasing to ~18.63 cm/ka during 6.72 – 5.11 ka BP (0.9m~0.6m). In the depth of 0.6 m to 0.4 m, this interval records an abrupt, extreme surge in sedimentation, reaching a peak rate of ~133.33 cm/ka over a brief period (5.11 – 4.96 ka BP). Following this pulse, the rate stabilizes at a lower level of ~4.96 cm/ka from 4.96 ka BP to the present.

The calculated sedimentation rate for Stage IV should be interpreted with caution due to the relatively large OSL dating uncertainties compared to the short time interval. The exact magnitude of the rate enhancement during this period remains constrained by methodological limitations, though the sedimentary record clearly indicates increased deposition and coarser input from proximal sources.

Table 2 Optically stimulated luminescence dating results of the ZYHPM01 profile.

Sample No	Profile depth	Grain size	U	Th	K	Equivalent dose	Environmental Dose Rate	Water content	Age Model	Age
	(m)	μm	(μg/g)	(μg/g)	(%)	(Gy)	(Gy/ka)	(%)		(ka)
ZYHPM01-0.2	0.2	125-180	2.86±0.11	11.7±0.51	1.73±0.02	12.60±1.69	2.63±0.09	29	CAM	4.80±0.65
ZYHPM01-0.6	0.6	125-180	3.16±0.14	13±0.45	1.77±0.01	14.83±2.25	2.90±0.10	23	FMM	5.11±0.77
ZYHPM01-0.9	0.9	125-180	3.23±0.16	12.8±0.43	1.82±0.02	19.44±0.71	2.90±0.10	25	CAM	6.72±0.25
ZYHPM01-1.1	1.1	125-180	2.96±0.12	12.7±0.63	1.92±0.03	28.42±0.98	2.88±0.09	28	CAM	9.86±0.35
ZYHPM01-1.5	1.5	125-180	2.59±0.08	11.8±0.49	2.06±0.01	32.80±3.54	2.82±0.10	28	FMM	11.63±1.25

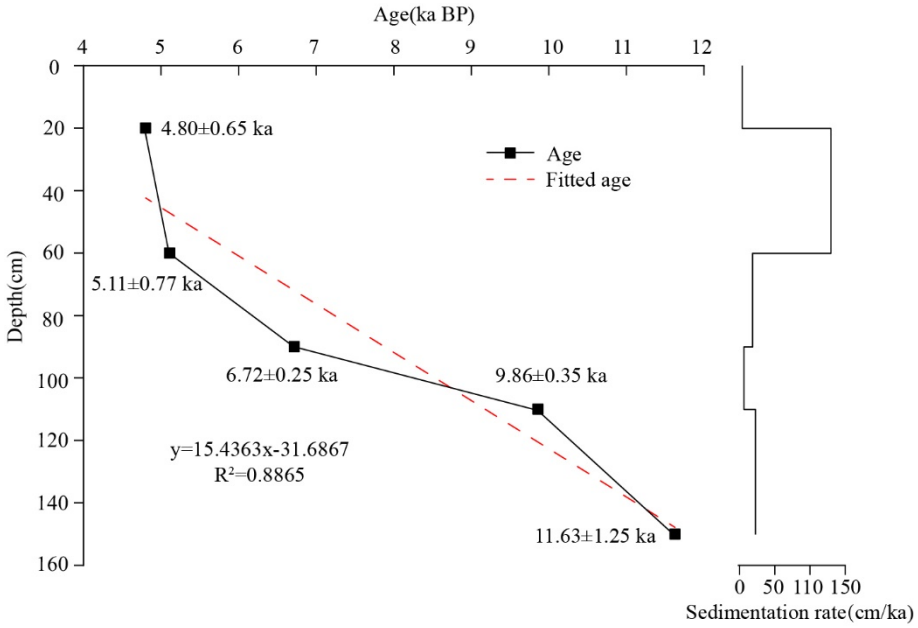

Fig. 3. Age-depth model of sediments from the ZYHPM01 profile.

3.3. Grain size characteristics

The sediments of the ZYHPM01 profile are predominantly composed of silt and clayey silt, with a generally minimal sand content (Table 3, Fig. 4). On the Shepard ternary diagram (Fig. 5a), samples cluster densely within the silt and clayey silt. Quantitative analysis shows that silt is the dominant fraction, with fine silt (4 – 16 μm) and medium silt (16–32 μm) accounting for averages of 39.47% and 23.35%, respectively. The clay content (<4 μm) averages 21.94%, while the sand fraction (>63 μm) is low, averaging 1.44%.

The vertical evolution of grain size parameters defines five distinct stratigraphic stages (Fig. 4). Stage I (1.6 – 1.2 m) exhibits a clear fining-upward sequence, where the median grain size (Md) decreases from 12.77 μm at the base to 9.84 μm at the top, accompanied by a rise in clay content from 18.74% to 23.54%. This transitions into the finest-grained interval of the profile, encompassing Stages II and III (1.2 – 0.6 m). During this period, the sediment texture remains stable and fine, with Md values fluctuating narrowly between 9.84 μm and 11.19 μm and clay content maintaining a high average of ~23%. A sharp textural discontinuity occurs in Stage IV (0.6 – 0.4 m), where the Md abruptly jumps from 10.53 μm to 12.31 μm, marking the onset of coarsening. This trend intensifies in Stage V (0.4 – 0 m), which contains the coarsest deposits in the profile (peak Md of 13.21 μm) and the highest sand content (up to 3.01%).

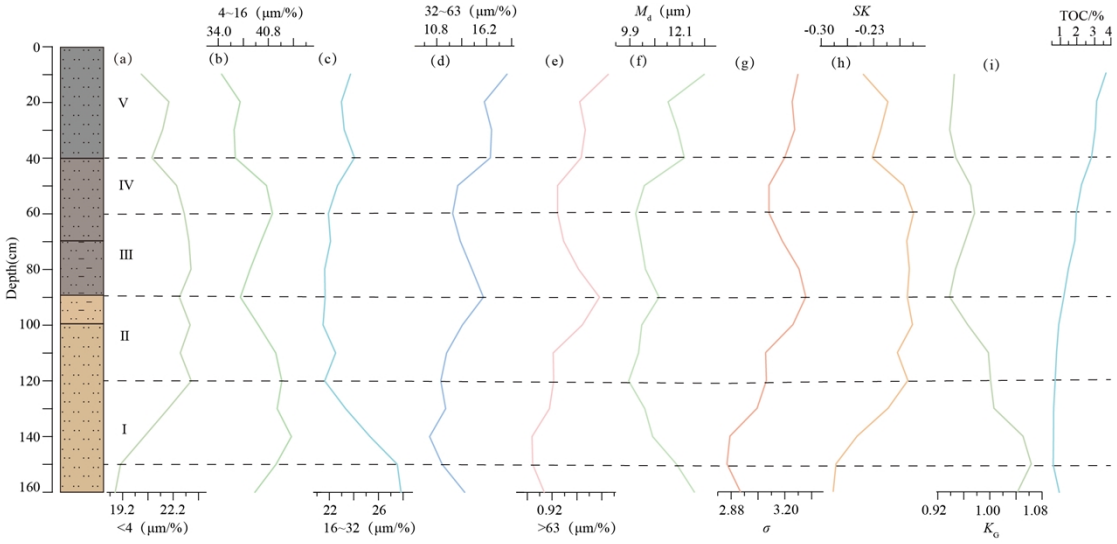

Fig. 4. Evolution curves of sediment grain size, granulometric parameters, and TOC.

These variations are further corroborated by statistical parameters and frequency distributions. The sorting coefficient (σ) ranges from 2.85 and 3.32, indicating generally poor sorting. Skewness (SK) values shift from near-symmetrical in finer layers to more positively skewed (-0.29 to 0.17) in coarser layers. The kurtosis (KG) remains close to mesokurtic (0.94 to 1.06). Frequency distribution curves (Fig. 6) display a transition from a bimodal pattern in the lower and middle sections (Stages I – III), with a primary peak in the coarse silt range, to a more complex trimodal distribution in the upper sections (Stages IV – V), where an additional fine sand population emerges, consistent with the abrupt coarsening observed in the standard grain-size metrics.

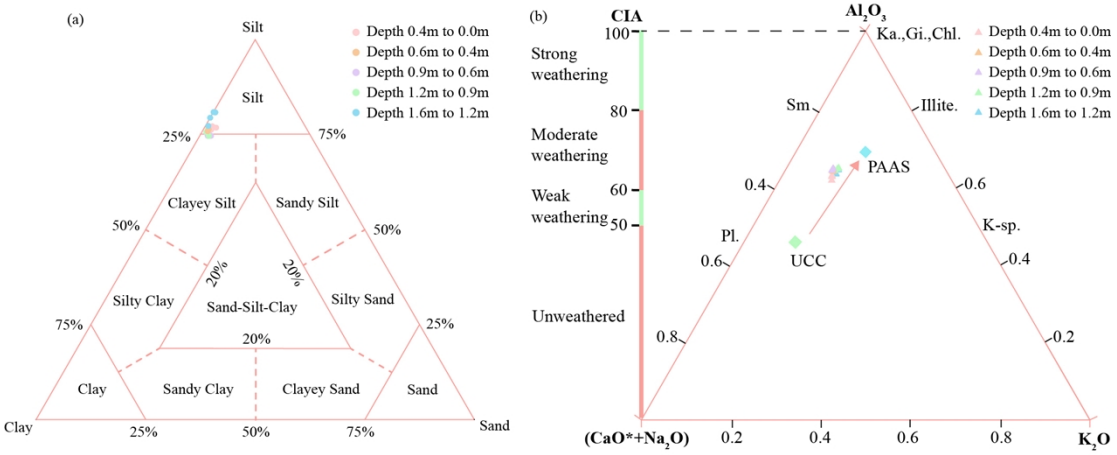

Fig. 5. (a) Shepard triangular diagram of sediment grain size and (b) A-CN-K triangular diagram of elements.

Table 3

Summary of contents and parameters of sediment grain size fractions.

Sample No	depth (m)	<4 μm (%)	4~16 μm (%)	16~32 μm (%)	32~63 μm (%)	>63 μm (%)	M_d (μm)	σ	SK	KG
L1	0.1	20.38	34.46	23.72	18.42	3.01	13.21	3.28	-0.24	0.95
L2	0.2	22.12	36.98	23.00	15.95	1.95	11.59	3.24	-0.21	0.94
L3	0.3	21.73	36.17	23.21	16.73	2.15	12.01	3.26	-0.22	0.94

L4	0.4	21.05	36.31	24.05	16.59	2.00	12.31	3.20	-0.23	0.95
L5	0.5	22.61	40.53	22.66	13.08	1.12	10.53	3.11	-0.18	0.97
L6	0.6	23.10	41.35	21.93	12.51	1.12	10.15	3.11	-0.17	0.98
L7	0.7	23.39	39.80	22.11	13.35	1.35	10.38	3.19	-0.18	0.96
L8	0.8	23.53	38.33	21.63	14.60	1.90	10.59	3.28	-0.18	0.95
L9	0.9	22.80	37.00	21.67	15.85	2.68	11.19	3.32	-0.18	0.94
L10	1	23.47	39.42	21.50	13.58	2.04	10.43	3.25	-0.17	0.97
L11	1.1	22.85	41.80	22.52	11.87	0.96	10.28	3.09	-0.19	1.00
L12	1.2	23.54	42.63	21.62	11.22	0.98	9.84	3.09	-0.18	1.00
L13	1.3	22.09	41.99	23.33	11.76	0.83	10.56	3.03	-0.21	1.01
L14	1.4	20.57	43.90	25.33	10.03	0.18	10.91	2.87	-0.25	1.05
L15	1.5	19.06	41.82	27.54	11.38	0.20	11.96	2.85	-0.28	1.06
L16	1.6	18.74	38.96	27.84	13.83	0.63	12.77	2.94	-0.29	1.04

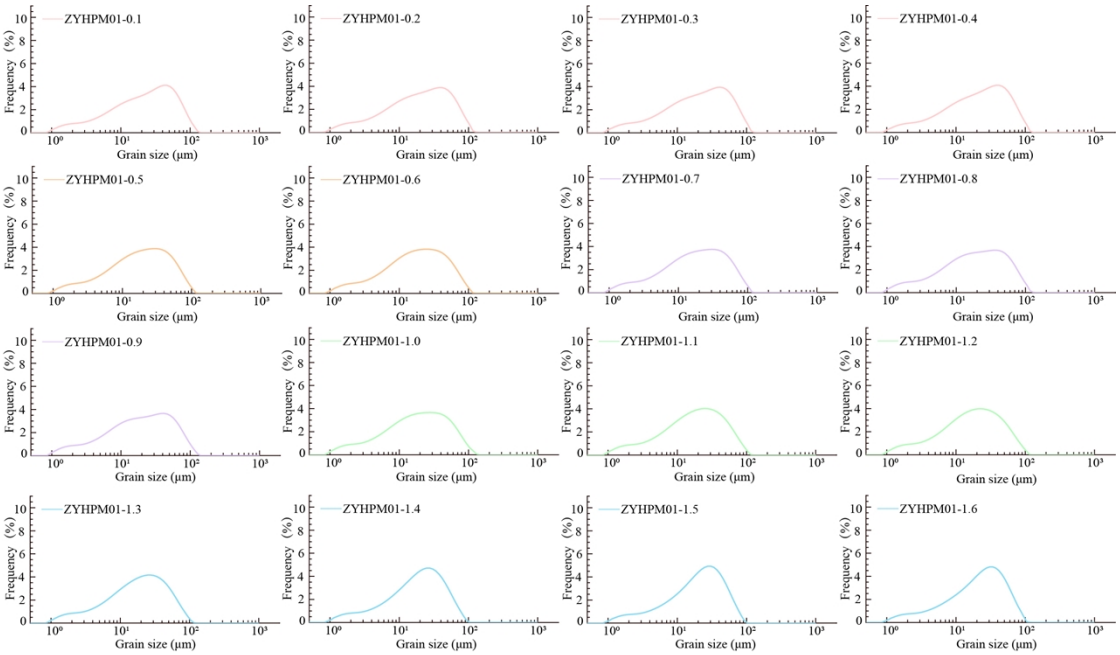

Fig. 6. Frequency curves of sediment grain size.

3.4. Grain size end-member modeling

Non-parametric end-member (EM) modeling successfully deconvolved the polymodal grain-size dataset into three robust components, explaining over 95% of the total variance ($R^2 > 0.95$, $\theta < 4.5°$; Fig. 7a, Fig. 7b). EM1 is the finest component, characterized by a modal grain size of 11.25 μm (fine silt) and a secondary peak in the clay fraction (<4 μm), with good sorting and a fine-grained positive skewness (Fig. 7c). EM2 represents an intermediate population with a modal size of 17.83 μm (medium silt), with moderate sorting (Fig. 7c). EM3 is the coarsest and most poorly sorted end-member, displaying a modal size of 31.69 μm (coarse silt), with a broad, asymmetrical distribution tailing towards the coarse end (Fig. 7c).

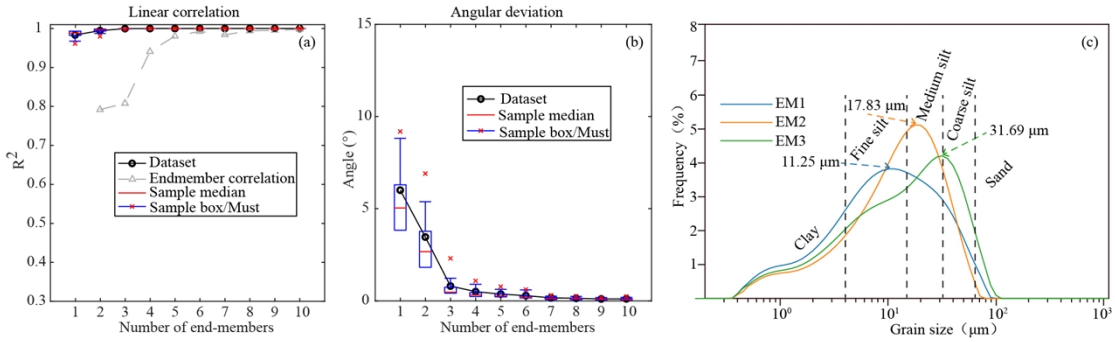

Fig. 7. Linear correlation, angular deviation, and EM grain size distribution curves of sediments.

The stratigraphic distribution of these components exhibits systematic variations (Fig. 8). In the lower to middle profile (Stages I – III; 1.6 – 0.6 m), the fine-grained EM1 is the dominant constituent. Within Stage I, the proportion of EM1 increases upwards, mirroring the fining-upward trend in median grain size. A fundamental compositional shift occurs at the boundary of Stage IV (0.6 m), marked by a sharp decline in EM1 and a concurrent, abrupt surge in the coarse-grained EM3. In the uppermost Stage V (0.4 – 0 m), the sedimentary assemblage is dominated by the coarser components (EM2 and EM3), which reach their maximum cumulative abundance, while the relative contribution of the fine-grained EM1 drops to its profile minimum.

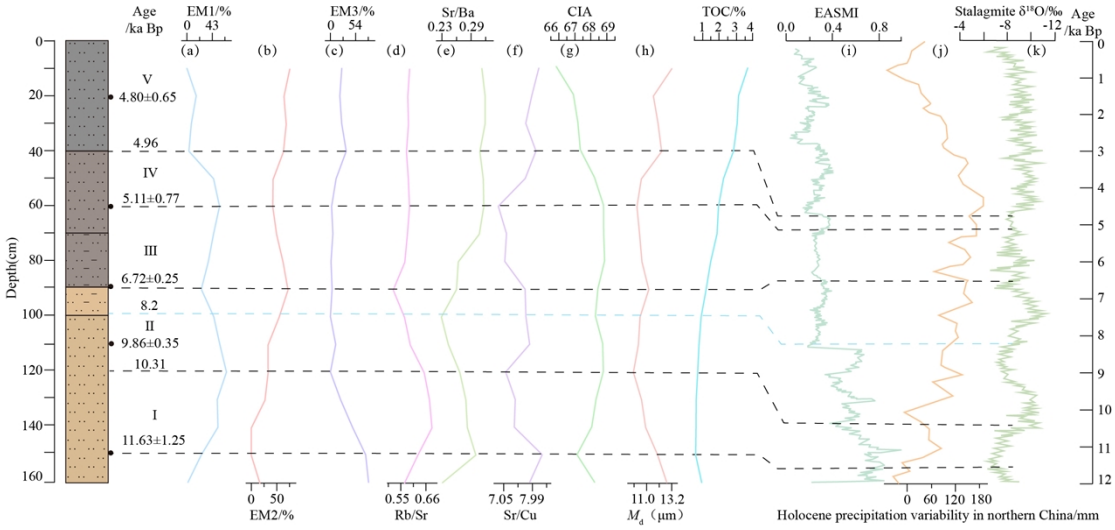

Fig. 8. Distribution curves of sediment grain size indices, element ratios, and their comparison with climate change proxy indices in other regions. (a) proportion of EM1, (b) proportion of EM2, (c) proportion of EM3, (d) Rb/Sr ratio, (e) Sr/Ba ratio, (f) Sr/Cu ratio, (g) chemical index of alteration, (h) median diameter of the grain size, (i) East Asian Summer Monsoon (EASM) intensity index (Lu et al., 2025), (j) Holocene precipitation variability in Northern China (Li et al., 2024), (k)$\delta^{18}O$ of Chinese cave stalagmite calcite from Sanbao (Wang et al., 2008).

3.5. Geochemical characteristics

The bulk geochemistry of the ZYHPM01 profile (Table 4) is dominated by SiO_2 (59.45%–63.30%, avg. 61.11%) and Al_2O_3 (13.54%–15.13%, avg. 14.47%), followed by TFe_2O_3 (4.96%–7.22%, avg. 5.95%). Mobile elements are relatively depleted, with CaO and Na_2O averaging 1.51%

and 1.81%, respectively. In the A-CN-K ternary diagram (Fig. 5b), all samples cluster tightly above the Post-Archean Australian Shale (PAAS) line, deviating from the Upper Continental Crust (UCC) composition towards the Al_2O_3 apex. Trace element ratios (e.g., La/Sc, Th/Sc) and chondrite-normalized REE patterns (Fig. 9, Table 5) exhibit high uniformity throughout the profile, characterized by LREE slight enrichment and negative Eu anomalies.

The vertical profiles of weathering and environmental proxies (CIA, Rb/Sr, Sr/Ba, Sr/Cu, and TOC) display distinct stage-dependent variations. During stage I (1.6 – 1.2 m), the CIA index increases steadily from 67.14 to 68.80. In contrast, the Rb/Sr ratio exhibits a convex trend, rising to a peak of 0.69 at 1.4 m before decreasing. Sr/Cu ratios show a gradual decline towards the top of the layer. Stage II (1.2 – 0.9 m) interval records a synchronous decline in weathering indices. Both CIA, Sr/Ba, and Rb/Sr drop to local minima. Conversely, Sr/Cu ratios exhibit an increasing trend. To stage III (0.9 – 0.6 m), the CIA values rebound and stabilize at high levels (avg. 68.81), accompanied by recoveries in the Rb/Sr and Sr/Ba ratios. This stage contains the highest TOC concentration rate in the profile, but the Sr/Cu ratio reaches its lowest values (avg. ~7.0). A sharp geochemical inflection occurs during stage IV (0.6 – 0.4 m). The Sr/Cu ratio increases rapidly, while Sr/Ba and Rb/Sr remain stable. The CIA drops abruptly to ~67.35. Despite this, TOC values show an increasing trend. And stage V (0.4 – 0 m), the Sr/Cu ratio continues to increase slightly, and CIA declines further to its profile minimum (65.83). These trends reflect the influence of cold-dry conditions during the Late Holocene, which enhanced physical erosion from proximal sources while limiting chemical weathering intensity. TOC values remain high, particularly in the surface layer, indicating effective preservation of organic matter under reduced microbial decomposition rates.

Table 4 Summary of sediment element contents and parameters. Element contents of the upper continental crust are from Taylor and McLennan (1985).

Depth (m)	SiO_2 (%)	Al_2O_3 (%)	TFe_2O_3 (%)	MgO (%)	CaO (%)	Na_2O (%)	K_2O (%)	TOC (%)	Ba (μg/g)	Cu (μg/g)	Rb (μg/g)	Sc (μg/g)	Sr (μg/g)	Th (μg/g)	CIA	La/Sc	Th/Sc	Rb/Sr	Sr/Ba	Sr/Cu
0.1	60.53	13.54	4.96	1.38	1.72	1.76	2.32	3.70	597.00	23.40	113.00	12.90	192.00	11.70	65.83	2.69	0.91	0.59	0.32	8.21
0.2	61.00	13.97	5.36	1.40	1.72	1.74	2.27	3.15	587.00	24.20	112.00	13.40	193.00	12.10	66.91	2.66	0.90	0.58	0.33	7.98
0.3	60.67	13.85	5.41	1.37	1.64	1.74	2.24	3.07	584.00	24.70	112.00	12.80	192.00	11.40	67.19	2.74	0.89	0.58	0.33	7.77
0.4	61.15	13.93	5.52	1.36	1.60	1.73	2.23	2.85	609.00	23.80	111.00	12.60	193.00	11.70	67.35	2.79	0.93	0.58	0.32	8.11
0.5	62.13	14.17	5.62	1.40	1.48	1.78	2.21	2.25	576.00	24.10	109.00	13.80	187.00	12.40	68.24	2.68	0.90	0.58	0.32	7.76
0.6	61.36	14.51	5.82	1.48	1.49	1.79	2.18	1.95	574.00	27.20	110.00	14.70	187.00	12.60	68.81	2.48	0.86	0.59	0.33	6.88
0.7	63.30	15.13	5.94	1.48	1.59	1.80	2.28	1.86	602.00	26.60	110.00	14.40	190.00	12.30	68.82	2.67	0.85	0.58	0.32	7.14
0.8	61.14	14.95	6.37	1.47	1.57	1.77	2.24	1.48	716.00	27.10	109.00	14.30	192.00	11.50	68.88	2.59	0.80	0.57	0.27	7.08
0.9	59.89	14.64	6.61	1.50	1.56	1.82	2.20	1.21	785.00	26.70	107.00	14.50	207.00	13.20	68.46	2.64	0.91	0.52	0.26	7.75
1	59.54	14.44	7.20	1.49	1.46	1.82	2.28	0.91	853.00	25.20	111.00	14.40	196.00	12.60	68.30	2.79	0.88	0.57	0.23	7.78
1.1	60.09	14.57	7.22	1.49	1.40	1.79	2.37	0.78	798.00	24.80	116.00	14.40	196.00	13.50	68.76	2.83	0.94	0.59	0.25	7.90
1.2	61.25	15.13	5.89	1.59	1.36	1.89	2.49	0.70	700.00	26.70	124.00	15.30	190.00	13.80	68.80	2.46	0.90	0.65	0.27	7.12
1.3	61.92	14.88	5.59	1.57	1.35	1.90	2.52	0.61	649.00	24.90	125.00	14.80	185.00	12.40	68.34	2.49	0.84	0.68	0.29	7.43
1.4	62.35	14.90	5.45	1.67	1.36	1.86	2.56	0.60	641.00	25.00	127.00	15.60	185.00	13.20	68.07	2.49	0.85	0.69	0.29	7.40
1.5	61.92	14.45	5.84	1.64	1.36	1.96	2.53	0.58	640.00	23.70	123.00	14.90	197.00	12.80	67.14	2.49	0.86	0.62	0.31	8.31
1.6	59.45	14.40	7.19	1.46	1.47	1.77	2.29	0.94	845.00	24.80	111.00	14.00	196.00	13.10	68.25	2.69	0.94	0.57	0.23	7.90
UCC	66.60	15.40	5.04	2.48	3.59	3.27	2.80	—	628.00	28	84.00	14.00	320.00	10.50	—	—	—	—	—	—

Table 5 Summary of sediment rare earth elements contents. Rare element contents of upper continental crust are from Taylor and McLennan (1985), PAAS are from Nance and Taylor (1976), NASC are from Haskin et al. (1966).

Depth/m	La	Ce	Pr	Nd	Sm	Eu	Gd	Tb	Dy	Ho	Er	Tm	Yb	Lu
	μg/g	μg/g	μg/g	μg/g	μg/g	μg/g	μg/g	μg/g	μg/g	μg/g	μg/g	μg/g	μg/g	μg/g
0.1	34.7	68.6	9.02	33.2	6.27	1.27	5.41	0.8	4.65	0.91	2.66	0.41	2.65	0.4
0.2	35.6	70.1	9.29	33.9	6.34	1.34	5.6	0.87	5.04	0.99	2.78	0.45	2.8	0.43
0.3	35.1	69.2	8.87	32.4	6.15	1.27	5.36	0.82	4.79	0.95	2.62	0.42	2.7	0.4
0.4	35.2	70.8	8.97	32.9	6.37	1.37	5.54	0.87	5.13	1.01	2.81	0.45	2.9	0.43
0.5	37	70.3	9.13	34.4	6.66	1.37	5.64	0.88	5.22	1	2.79	0.47	2.9	0.42
0.6	36.4	73	9.33	34.6	6.68	1.38	5.98	0.9	5.33	1.04	2.79	0.46	2.91	0.43
0.7	38.4	71.6	9.26	34.8	6.67	1.4	5.7	0.92	5.21	1.02	2.78	0.46	2.87	0.44
0.8	37.1	69.4	9.15	34.1	6.39	1.4	5.78	0.91	5.02	0.98	2.83	0.44	2.82	0.42
0.9	38.3	79.4	9.81	36.6	6.95	1.44	6	0.91	5.3	1.03	2.94	0.48	2.99	0.45
1	40.2	78.5	9.59	35	6.81	1.46	5.99	0.89	5.26	1.04	2.91	0.47	3.01	0.45
1.1	40.8	81.7	9.93	37.7	7.14	1.49	6.2	0.99	5.57	1.12	2.85	0.49	3.13	0.47
1.2	37.7	77.2	9.64	36	6.91	1.46	6.15	0.97	5.59	1.11	3.07	0.5	3.21	0.48
1.3	36.8	75.6	9.24	34.4	6.55	1.37	5.68	0.91	5.28	1.01	2.82	0.45	2.97	0.43
1.4	38.8	78.4	9.66	35.5	6.72	1.42	5.92	0.95	5.47	1.04	2.91	0.48	3.1	0.46
1.5	37.1	77	9.48	35.1	6.91	1.4	5.78	0.93	5.4	1.05	2.98	0.49	3.14	0.46
1.6	37.6	75.9	9.14	35.1	6.77	1.48	6.01	0.97	5.58	1.11	3.01	0.48	3.09	0.46
UCC	31	63	7.1	27	4.7	1	4	0.7	3.9	0.83	2.3	0.3	1.96	0.31
PAAS	38	79.6	8.83	33.9	5.55	1.08	4.66	0.77	4.68	0.99	2.85	0.41	2.82	0.43
NASC	32	73	7.9	31	5.7	1.24	5.21	0.85	5.8	1.04	3.4	0.5	3.1	0.48

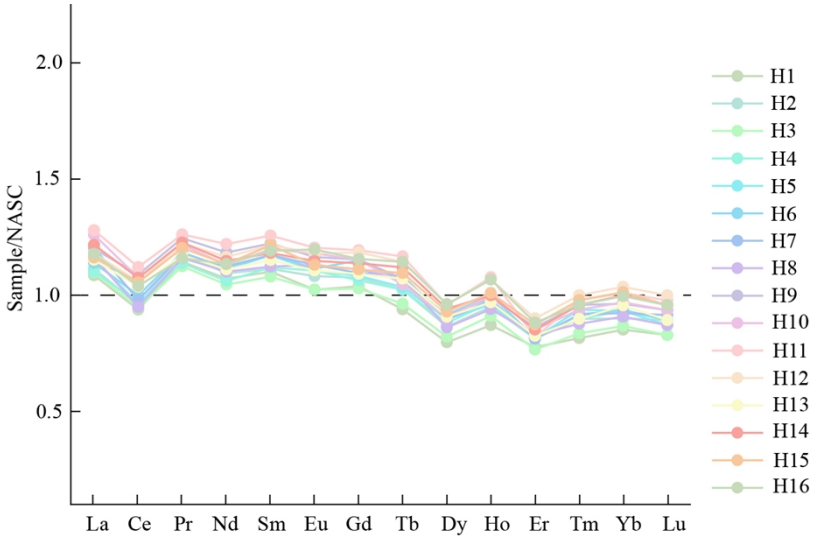

Fig. 9. Distribution curves of rare earth elements in sediments.

4. Discussion

4.1. Reliability of chronology and stability of provenance

A prerequisite for paleoenvironmental reconstruction in soil profiles is establishing a robust chronology and excluding the interference of provenance shifts. In black soils, however, this is often complicated by intense pedoturbation, which mixes soil particles and blurs depositional signals (Zhang et al., 2024a). To validate our chronological framework, we implemented a multi-faceted verification strategy: 1) Unlike

studies relying on fine silt (4 – 11 μm), which is susceptible to downward translocation via illuviation or bioturbation, we extracted coarse-grained quartz (125 – 180 μm) for OSL dating. Coarser grains are physically resistant to vertical migration within the soil matrix, thereby preserving the primary stratigraphic order (Bateman et al., 2003; Kristensen et al., 2015); 2) a rigorous statistical approach to the OSL data was applied (in 3.2). For samples exhibiting broad or multi-modal equivalent dose (De) distributions (e.g., at 0.6 m and 1.5 m), the Finite Mixture Model (FMM) was applied to statistically isolate the primary depositional population from intrusive grains (Galbraith and Green, 1990); 3) The resulting ages (4.80 – 11.63 ka) follow a strict stratigraphic sequence with no reversals (Fig. 3). Moreover, the preservation of sharp lithological boundaries—specifically the abrupt textural coarsening at the Stage III/IV transition—provides compelling physical evidence that post-depositional homogenization was limited and did not obliterate high-frequency sedimentary events; 4) The reliability of the chronology is further reinforced by comparative analysis with regional records (Fig. 10). While raw depth-series grain size records across the Songnen Plain often appear spatially heterogeneous due to geomorphic controls on sedimentation rates (e.g., leeward vs. windward deposition), isochronous alignment reveals a coherent regional signal. Notably, the ~6.5 ka horizon emerges as a pivotal regional isochron: it marks not only the widespread onset of black soil formation (Cui et al., 2021; Yang et al., 2023), but also a critical granulometric turning point where sediments consistently fine upwards and downwards across multiple profiles. Furthermore, the temporal evolution of grain size in our profile, characterized by "mid-Holocene fining" followed by "late-Holocene coarsening," aligns perfectly with high-resolution regional records (Fig. 10). This astounding temporal consistency confirms that the ZYHPM01 profile faithfully records broad-scale climatic evolution rather than localized geomorphic noise.

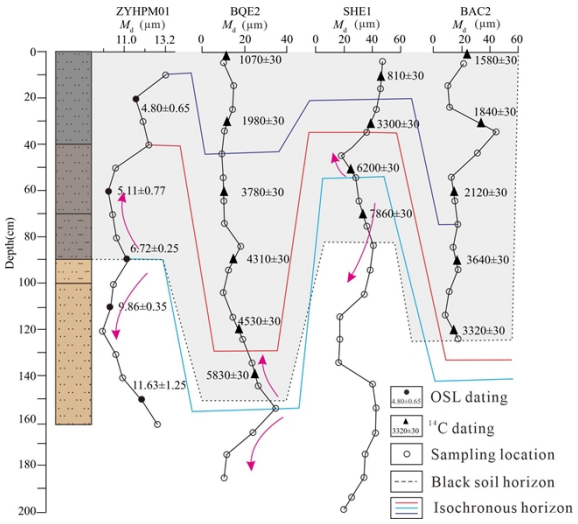

Fig. 10. Comparative chart of median grain size of Holocene strata in the eastern Songnen Basin (data of BQE2, etc. from Zhang et al., 2024b)

Regarding provenance, the geochemical data confirm a stable source throughout the Holocene. The chondrite-normalized REE patterns (Fig. 9) exhibit remarkable uniformity, and diagnostic trace element ratios (e.g., La/Sc, Th/Sc) show narrow variations aligning with the Upper Continental Crust (UCC) (Taylor and McLennan, 1985; Gallet et al., 1996). This homogeneity implies that the observed variations in grain size and weathering proxies are driven by climatic dynamics rather than shifts in source lithology.

4.2. Paleoenvironmental significance of sedimentary proxies and weathering indices

To accurately reconstruct the Holocene evolution, it is essential to interpret the specific environmental processes governing physical and chemical proxies in the ZYHPM01 profile. The three grain-size end-members (EMs) characterize distinct aerodynamic transport modes. EM1 (fine silt, modal ~11.25 μm) represents the background dust component transported via high-altitude suspension, similar to typical Chinese loess (e.g. Harbin loess; Pye, 2015; Song et al., 2023; Sun et al., 2003; Tsoar and Pye, 1987). EM2 (medium silt, modal ~17.83 μm) represents a coarser regional dust component from nearby sources such as Horqin and Songnen Sand Lands (Li et al., 2025; Sun et al., 2003; Xie et al., 2019; Zhang et al., 2024b). The relative increase of EM2 during colder periods (e.g., Stage II and Stage V) reflects activation of these dune systems driven by a strengthened winter monsoon (An et al., 2012). EM3 (coarse silt, modal ~31.69 μm) indicates proximal high-energy saltation events associated with strong winter monsoon outbreaks or localized surface reworking. Its multimodal distribution (Fig. 7c) and dominance during abrupt transitions (e.g., Stage I and Stage IV) suggest a complex genesis, such as snowmelt and rainfall wash (Bullard and McTainsh, 2003; Vandenberghe, 1993; Gillette and Walker, 1977; Goossens and Rajot, 2008).

Geochemically, the CIA reliably tracks the intensity of silicate weathering, specifically transformation of feldspar to clay minerals (Nesbitt and Young, 1982; Fedo et al., 1995). The Rb/Sr ratio is controlled by a competition between leaching (loss of mobile Sr) and retention (adsorption of Rb on clay minerals) (Gallet et al., 1996; Chen et al., 1999). The Sr/Cu ratio provides a sensitive indicator of the balance between physical erosion and chemical weathering. Strontium is primarily hosted in plagioclase feldspars, which are abundant in physical detritus but rapidly depleted by chemical weathering, whereas Copper is typically retained in clay minerals and organic complexes (Roberts et al., 2008; Jin et al., 2010). Consequently, a low Sr/Cu ratio signifies intense chemical leaching in warm-humid environments, while elevated Sr/Cu indicates increased physical erosion under cold-dry conditions (Sheldon and Tabor, 2009). TOC concentrations reflect the net result of biomass production (controlled by hydroclimate) and preservation potential (controlled by burial rate and temperature), rather than productivity alone (Schmidt et al., 2011; Dungait et al., 2012). In the ZYHPM01 profile, TOC variations are influenced by multiple factors, including climate-controlled vegetation productivity, sedimentation rate, and post-depositional preservation conditions.

4.3. Holocene climate evolution and environmental drivers

The integration of chronology, grain-size EM, and multi-proxy geochemical records reconstructs a dynamic history of environmental evolution in the eastern Songnen Plain, driven by the interplay between the East Asian Summer Monsoon (EASM) and sediment supply. This evolution is delineated into five distinct stages.

Stage I, Early Holocene (11.63 – 10.31 ka BP), was a period of rapid accumulation and incipient weathering. Following the termination of the Last Glacial Period, the region experienced rapid warming and increasing humidity associated with the strengthening EASM (Fig. 8; Dykoski et al., 2005; Wang et al., 2008). This stage is characterized by a high sedimentation rate (~22.73 cm/ka) and the dominance of fine-

grained distal dust (EM1). Geochemically, a distinct decoupling is observed: while the CIA rises continuously, the Rb/Sr ratio exhibits a convex pattern, peaking at 1.4 m. This trajectory reflects a transition from a "transport-limited" to a "weathering-limited" regime. Initially, high Rb/Sr ratios were driven by the adsorption of Rb on fine clay particles; however, as precipitation intensified, the selective leaching of mobile Sr outpaced Rb retention, initiating a decline in the ratio (Nesbitt and Young, 1982). This stage established the hydrothermal foundation for subsequent soil development.

Stage II, the Early-to-Middle Holocene transition (10.31 – 6.72 ka BP), was characterized by a climatic setback and weathering regression. Although the sampling resolution of this study precludes the precise pinning of short-term abrupt events, the broad stratigraphic trend of this interval is consistent with the environmental impacts of high-latitude cooling episodes, most notably the 8.2 ka BP event (Alley et al., 1997; Morrill et al., 2013). The sedimentation rate dropped to ~8.36 cm/ka, and the input of coarser proximal dust (EM2) increased, indicating a strengthening of the winter monsoon. Geochemically, this deterioration is evidenced by a synchronous decline in both CIA and Rb/Sr ratios to their profile minima. Concurrently, Sr/Cu ratios exhibited an increasing trend, suggesting that the influx of coarser, less-weathered material physically diluted the pedogenic signal, while cooler, drier conditions inhibited chemical alteration. This stage signifies a "pause" in soil formation, where physical erosion temporarily overwhelmed chemical weathering processes.

Stage III, the Mid-Holocene climatic optimum (6.72 – 5.11 ka BP), represents the Holocene Climatic Optimum (Mayewski et al., 2004), providing the ideal window for black soil formation (initiated at ~6.72 ka BP; Zhang et al., 2024a). Sedimentologically, this period is defined by the minimal contribution of coarse proximal dust (low EM2 and EM3) and the dominance of the fine-grained EM1 component. The significant reduction in median grain size (Md) reflects a stable landscape with weakened winter monsoon winds, which minimized physical erosion and allowed for sustained pedogenesis (Cui et al., 2021; Yang et al., 2023). Under peak EASM conditions (Berger and Loutre, 1991), the Sr/Cu ratio dropped to its lowest levels (avg. ~7.0), confirming intense chemical leaching in a warm-humid environment. The CIA peaked and stabilized, while the Rb/Sr ratio rebounded due to Rb retention in secondary clays. Most significantly, this stage records the profile's fastest rate of TOC accumulation. The coupling of high TOC with high CIA indicates that dense vegetation cover and vigorous pedogenesis promoted the formation of organo-mineral complexes, which protected organic carbon from mineralization (Kögel-Knabner, 2002).

Stage IV, Mid-to-Late Holocene transition (5.11 – 4.96 ka BP), records a brief interval of enhanced sedimentation and environmental transition. The rapid coarsening of sediment, marked by increases in EM2 and EM3 components, reflects increased input from proximal sources during a period of climatic instability. The enhanced sedimentation during this interval likely resulted from localized geomorphic processes—including episodic dune activation, surface runoff events, or extreme aeolian activity—superimposed on broader Holocene climate changes. The environmental shift during this period coincides with a major Holocene climate transition event documented at ~4.2 ka BP (Weiss, 2016), which affected monsoon regions globally and has been associated with widespread drought conditions in East Asia. The sedimentation rate surged to approximately 130 cm/ka, accompanied by a sharp increase in coarse-grained EM2 and EM3

components. These changes reflect a major shift in depositional regime, with enhanced input from proximal sources during a period of climatic instability. Concurrently, the Sr/Cu ratio increased rapidly, reflecting the dominance of fresh, less-weathered material. The CIA values declined during this interval, indicating reduced chemical weathering intensity under the deteriorating climatic conditions. Notably, TOC values exhibited an increasing trend alongside declining CIA, which may be attributed to the rapid burial effect: the extreme sedimentation rate effectively sealed contemporaneous organic matter from atmospheric oxidation, preserving it within the rapidly accreting soil layer.

Stage V, the Late Holocene (4.96 ka BP to present), was a period of cold-dry preservation and topsoil pedogenesis. Under the persistent dominance of the winter monsoon, the landscape entered a phase of stable aeolian accretion under cold and dry conditions, aligning with the "Neoglacial" cooling (Grove, 2004; Chen et al., 2015). Sedimentologically, this stage is characterized by a resurgence of coarse-grained components (EM2 and EM3), which reach their highest cumulative abundance in the profile. The elevated median grain size reflects intensified regional winds and frequent proximal dust storms, marking a shift from chemical to mechanical dominance. Consequently, the geochemical suite (low CIA, stable Sr/Ba) reflects a "kinetic-limited" weathering regime where physical input outpaces alteration. Despite this, TOC continued to rise, reaching high levels in the surface layer. This decoupling (High TOC vs. Low CIA) may be driven by two factors: (1) Temperature-Controlled Preservation, where cooling inhibited microbial decomposition rates more than primary productivity; and (2) Active Root Zone Input, representing modern biological additions to the Mollic epipedon (Cui et al., 2021).

4.4. Mechanism of black soil formation

The formation of black soils in the eastern Songnen Plain is revealed not as a simple product of weathering, but as a complex "multi-source and multi-process" system driven by the interplay of accretionary deposition and climatic modulation. The fundamental material basis is established by the continuous influx of distal background dust (EM1), which exhibits uniform geochemical characteristics comparable to the Upper Continental Crust (UCC) and typical loess deposits (Gao et al., 1998; Sun et al., 2003; Song et al., 2023). This fine-grained substrate provides the necessary specific surface area for organic matter adsorption. However, this foundation is dynamically modified by regional surface processes. As indicated by the end-member modeling, episodic inputs of coarser proximal dust (EM2 and EM3) from nearby sand lands (e.g., Horqin and Songnen) occurred during cold-dry intervals (Li et al., 2024; Xie et al., 2019). The multimodal distribution of the coarsest component (EM3) further suggests that, beyond aeolian transport, localized surface reworking events, such as snowmelt runoff and rainfall wash, contributed to the physical mixing of the parent material (Bullard and McTainsh, 2003; Vandenberghe, 1993).

The transformation of these sediments into fertile black soil was critically dependent on a specific "environmental window" during the Mid-Holocene (Stage III). This period records the most intense chemical alteration throughout the Holocene sequence. The CIA values peaked at approximately 68.8, significantly above the profile average, while the Sr/Cu ratio dropped to its minimum (~7.0). These geochemical signatures confirm a regime dominated by intense silicate weathering and leaching under warm-humid

conditions (Fedo et al., 1995; Nesbitt and Young, 1982). The warm and humid environment facilitated the decomposition of primary minerals and the formation of secondary clay minerals through pedogenic processes. These secondary minerals, together with high biological activity, promoted the formation of stable organo-mineral complexes that are essential for sequestration of soil organic carbon (Kögel-Knabner, 2002). Thus, the Mid-Holocene Climatic Optimum represents the critical period when intense chemical weathering, enhanced biological productivity, and active pedogenesis combined to establish the distinctive properties of black soil in the Songnen Plain.

Regarding the timing of formation, the multi-proxy records indicate that mature black soil development was initiated at ~6.72 ka BP. This timing aligns well with the "accretionary pedogenesis" model (Yang et al., 2023; Zhang et al., 2024a), which posits that black soils thicken upwards synchronously with Holocene dust deposition. While Cui et al. (2021) suggested an earlier onset (no later than 8.5 ka BP) based on ^{14}C dating, the integration of grain-size and geochemical data in this study suggests a nuance: while sediment accumulation began earlier (Stage I and II), the distinct physicochemical properties of the black soil (e.g., peak clay retention and TOC accumulation) were only fully established during the Mid-Holocene Climatic Optimum. Therefore, although the "material body" of the soil is time-transgressive, its "pedogenic identity" is a product of the climatic optimum.

Finally, the persistence of this organic-rich layer is attributed to a distinct "Formation-Preservation Coupling" mechanism. The multi-proxy records reveal that the timing of peak chemical weathering (Stage III) does not perfectly align with the highest TOC retention (Stages IV-V). We propose that the Mid-Holocene acted as the "Formation Phase," providing the hydrothermal conditions for intense biomass production and mineral transformation. Crucially, the subsequent environmental deterioration served as the "Preservation Phase." The shift to a cold and dry climate in the Late Holocene acted as a "climatic lock," which significantly inhibited microbial respiration and restricted chemical leaching (Cui et al., 2021). Thus, the modern black soil resource in the Songnen Plain represents a legacy of peak Mid-Holocene productivity that was kinetically fossilized by the Late Holocene climatic cooling.

4.5. Limitations of the research

This study has several limitations that should be considered when interpreting the results. First, the findings are derived primarily from a single sediment profile, which restricts the ability to fully capture spatial variability across the Songnen Plain. Second, the sampling resolution of 10 cm, while suitable for identifying millennial-scale trends, is insufficient to resolve centennial-scale climatic events. This limits the detection of short-term environmental fluctuations that may have influenced pedogenesis and dust deposition. Third, interpretation of certain proxies involves inherent complexity. For example, while CIA is a robust indicator of chemical weathering intensity, it can be influenced by variations in sediment provenance and source lithology. However, the relatively stable La/Sc and Th/Sc ratios throughout the profile suggest a consistent source, supporting the interpretation of CIA variations as primarily reflecting changes in weathering intensity. Finally, the chronology relies on a limited number of OSL dates, which affects the precision of the age – depth model, particularly around potential hiatuses (e.g., near 100 cm depth). These

constraints highlight the need for higher-resolution, multi-profile studies in the future to better quantify regional heterogeneity and short-term climate dynamics. The sedimentation rate calculated for Stage IV represents a statistical outlier compared to other Holocene stages, being approximately an order of magnitude higher than the profile average. This anomaly results from the relatively short time interval between OSL dating points, which amplifies the influence of dating uncertainties on rate calculations. While Stage IV clearly indicates enhanced deposition during a brief period, the exact magnitude of the rate increase should be treated with caution. Future studies with higher sampling density would be necessary to better resolve sedimentation dynamics during this interval.

5. Conclusions

This study reconstructs the Holocene evolution history of black soil in the eastern Songnen Plain by establishing a robust chronostratigraphic framework using coarse-grained quartz OSL dating, integrated with grain-size end-member modeling and multi-proxy geochemical analysis. The results demonstrate that the parent material comprises a dynamic mixture of stable distal background dust (EM1) and episodic proximal aeolian inputs (EM2 and EM3) from regional sand lands.

The paleoenvironmental evolution unfolded through distinct phases governed by the East Asian Monsoon. Following rapid accumulation during the Early Holocene, the region experienced a climatic setback during the transition to the Middle Holocene, broadly consistent with high-latitude cooling episodes such as the 8.2 ka event. The subsequent Mid-Holocene Climatic Optimum (6.72 – 5.11 ka BP) established warm and humid conditions, serving as the primary environmental window for intense pedogenesis and black soil initiation. This period was terminated by an abrupt shift to cold-dry conditions during the Late Holocene, characterized by enhanced coarse-grained dust inputs driven by a strengthened winter monsoon.

The genesis of the thick, organic-rich black soil is revealed as a process of accretionary pedogenesis, driven by a Formation-Preservation mechanism. We propose that the Mid-Holocene Climatic Optimum provided optimal climatic conditions for intense chemical weathering, high biological productivity, and active pedogenesis ("Formation Phase"). Subsequently, the transition to a cold and dry climate during the Late Holocene inhibited microbial decomposition and restricted chemical leaching, thereby effectively preserving the accumulated organic carbon within the aggrading soil profile. This temporal coupling suggests that the modern black soil resource in the Songnen Plain represents a legacy of peak Mid-Holocene productivity that was preserved by climatic deterioration. These findings provide important implications for understanding critical zone evolution and the long-term response of soil systems to Holocene climate change at monsoon margins.

Declaration of Competing Interest

None.

Acknowledgements

This work is financially supported by the China Geological Survey Project (Grants No. DD20242396, DD20211589, DD20240008) and the funding project of Northeast Geological S&T Innovation Center, China Geological Survey (Grant No. QCJJ2023-31).

References

Aitken, M.J., Smith, B.W., 1988. Optical dating: Recuperation after bleaching. Quat. Sci. Rev. 7(3), 387-393.

Alley, R.B., Mayewski, P.A., Sowers, T., Stuiver, M., Taylor, K.C., Clark, P.U., 1997. Holocene climatic instability: A prominent, widespread event 8200 yr ago. Geology 25(6), 483-486.

An, Z., Colman, S.M., Zhou, W., Li, X., Brown, E.T., Jull, A.J.T., Cai, Y., Huang, Y., Lu, X., Chang, H., Song, Y., Sun, Y., Xu, H., Liu, W., Jin, Z., Liu, X., Cheng, P., Liu, Y., Ai, L., Li, X., Liu, X., Yan, L., Shi, Z., Wang, X., Wu, F., Qiang, X., Dong, J., Lu, F., Xu, X., 2012. Interplay between the Westerlies and Asian monsoon recorded in Lake Qinghai sediments since 32 ka. Sci. Rep. 2(1), 619.

Bateman, M.D., Frederick, C.D., Jaiswal, M.K., Singhvi, A.K., 2003. Investigations into the potential effects of pedoturbation on luminescence dating. Quat. Sci. Rev. 22(10), 1169-1176.

Berger, A., Loutre, M.F., 1991. Isolation values for the climate of the last 10 million years. Quat. Sci. Rev. 10(4), 297-317.

Bullard, J.E., McTainsh, G.H., 2003. Aeolian-fluvial interactions in dryland environments: examples, concepts and Australia case study. Prog. Phys. Geogr. 27(4), 471-501.

Chen, J., An, Z., Head, J., 1999. Variation of Rb/Sr Ratios in the Loess-Paleosol Sequences of Central China during the Last 130,000 Years and Their Implications for Monsoon Paleoclimatology. Quat. Res. 51(3), 215-219.

Chen, F., Xu, Q., Chen, J., Birks, H.J.B., Liu, J., Zhang, S., Jin, L., An, C., Telford, R.J., Cao, X., Wang, Z., Zhang, X., Selvaraj, K., Lu, H., Li, Y., Zheng, Z., Wang, H., Zhou, A., Dong, G., Zhang, J., Huang, X., Bloemendal, J., Rao, Z., 2015. East Asian summer monsoon precipitation variability

since the last deglaciation. Sci. Rep. 5(1), 11186.

Chen, Y.Y., Yang, K., Yu, J.B., Zhang, Q.P., Yang, Z.W., Liu, X., Liu, J.C., Wang, C.C., 2024. Quaternary strata lithological characteristics and environmental geological significance of borehole WKZK01 in the eastern Songnen Plain. J. Geomech. 30(6), 952-964 (in Chinese with English abstract).

Cheng, L., Song, Y., Li, Y., Zhang, Z., 2018. Preliminary application of grain size end member model for dust source tracing of Xinjiang Loess and paleoclimate reconstruction. Acta Sedimentol. Sin. 36(6), 1148-1156 (in Chinese with English abstract).

Cui, J., Guo, L., Chen, Y., Wang, h., Yang, s., Xiong, S., 2021. Spatial distribution of 14C age and depth of mollisol sections in the Songnen Plain during the Holocene. Quaternary Sci. 41(5), 1332-1341 (in Chinese with English abstract).

Dallmeyer, A., Claussen, M., Wang, Y., Herzschuh, U., 2013. Spatial variability of Holocene changes in the annual precipitation pattern: a model-data synthesis for the Asian monsoon region. Clim. Dyn. 40(11), 2919-2936.

Dietze, E., Hartmann, K., Diekmann, B., Ijmker, J., Lehmkuhl, F., Opitz, S., Stauch, G., Wünnemann, B., Borchers, A., 2012. An end-member algorithm for deciphering modern detrital processes from lake sediments of Lake Donggi Cona, NE Tibetan Plateau, China. Sediment. Geol. 243-244, 169-180.

Dungait, J.A.J., Hopkins, D.W., Gregory, A.S., Whitmore, A.P., 2012. Soil organic matter turnover is governed by accessibility not recalcitrance. Global Change Biol. 18(6), 1781-1796.

Dykoski, C.A., Edwards, R.L., Cheng, H., Yuan, D., Cai, Y., Zhang, M., Lin, Y., Qing, J., An, Z., Revenaugh, J., 2005. A high-resolution, absolute-dated Holocene and deglacial Asian

monsoon record from Dongge Cave, China. Earth Planet. Sci. Lett. 233(1), 71-86.

Fedo, C.M., Wayne Nesbitt, H., Young, G.M., 1995. Unraveling the effects of potassium metasomatism in sedimentary rocks and paleosols, with implications for paleoweathering conditions and provenance. Geology 23(10), 921-924.

Folk, R.L., Ward, W.C., 1957. Brazos River bar [Texas]; a study in the significance of grain size parameters. J. Sediment. Res. 27(1), 3-26.

Galbraith, R.F., Green, P.F., 1990. Estimating the component ages in a finite mixture. Int. J. Radiat. Appl. Instrum. Part D 17(3), 197-206.

Gallet, S., Jahn, B.-m., Torii, M., 1996. Geochemical characterization of the Luochuan loess-paleosol sequence, China, and paleoclimatic implications. Chem. Geol. 133(1), 67-88.

Gao, S., Luo, T.C., Zhang, B.R., Zhang, H.F., Han, Y.w., Zhao, Z.D., Hu, Y.K., 1998. Chemical composition of the continental crust as revealed by studies in East China. Geochim. Cosmochim. Acta 62(11), 1959-1975.

Gillette, D.A., Walker, T.R., 1977. Characteristics of airborne particles produced by wind erosion of sandy soil, high plains of West Texas. Soil Sci. 123(2), 97-110.

Goossens, D., Rajot, J.L., 2008. Techniques to measure the dry aeolian deposition of dust in arid and semi-arid landscapes: a comparative study in West Niger. Earth Surf. Processes Landforms 33(2), 178-195.

Grove, J.M., 2004. The Little Ice Age (2nd edition). Routledge, Longdon.

Han, X., Li, N., 2018. Research progress of black soil in Northeast China. Sci. Geogr. Sin. 38(7), 1032-1041 (in Chinese with English abstract).

Haskin, L.A., Frey, F.A., Schmitt, R.A., Smith, R.H., 1966. Meteoritic, solar and terrestrial rare-earth

distributions. Phys. Chem. Earth. 7, 167-321.

Hou, X.R., Xie, Y.Y., Kang, C.G., Chi, Y.P., Wu, P., Sun, L., Sun, Y., Sun, J.H., 2023. Sedimentological characteristics of the Baitushan formation in the eastern foothills of the Great Xing'an Range: implications for stratigraphic divisions. Acta Sedimentol. Sin. 41(3), 720-734 (in Chinese with English abstract).

Jin, Z., Wang, S., Zhang, F., Shi, Y., 2010. Weathering, Sr fluxes, and controls on water chemistry in the Lake Qinghai catchment, NE Tibetan Plateau. Earth Surf. Processes Landforms 35(9), 1057-1070.

Kögel-Knabner, I., 2002. The macromolecular organic composition of plant and microbial residues as inputs to soil organic matter. Soil Biol. Biochem. 34(2), 139-162.

Kristensen, J.A., Thomsen, K.J., Murray, A.S., Buylaert, J.-P., Jain, M., Breuning-Madsen, H., 2015. Quantification of termite bioturbation in a savannah ecosystem: Application of OSL dating. Quat. Geochronol. 30, 334-341.

Li, J.H., Hou, H.X., Wang, W., Ren, B.Z., Zhang, G.G., Li, M., Qi, L., Du, X., Shi, L.F., Zhan, Z.D., Xi, G.Y., 2025. Geochemical characteristics of the ground substrate layer in the black soil area of the Northern Songnen Plain and its implications for the provenance of black soil. Acta Geosci. Sin. 46(4), 827-840 (in Chinese with English abstract).

Li, M., Xi, X., Xiao, G., Cheng, H., Yang, Z., Zhou, G., Ye, J., Li, Z., 2014. National multi-purpose regional geochemical survey in China. J. Geochem. Explor. 139, 21-30.

Li, Q., Wu, H., Cheng, J., Zhang, W., Yu, Y., Sun, A., Luo, Y., 2024. Hydroclimatic changes in eastern China during the Holocene based on pollen data and climate modeling. Global Planet. Change 234, 104391.

Liu, K., Song, Y., Du, S., Xiao, H., Chen, C., Xu, J., Dai, H., Fang, N. 2025. Spatiotemporal patterns and drivers of soil organic carbon in black soil landscapes of Northeast China. PLoS One, 20(6), e0320784.

Lu, S., Wu, L., Ma, C., Shu, J., Guan, H., Han, X., Luo, W., Xu, Z., Liu, B., Cai, W., Zhang, Y., Wei, Q., 2025. High- and low-latitude forcings on East Asian summer monsoon variability over the past 36,000 years: A high-resolution record from Lake Chaohu, eastern China. Sci. China Earth Sci. 68(6), 1921–1936.

Mayewski, P.A., Rohling, E.E., Curt Stager, J., Karlén, W., Maasch, K.A., David Meeker, L., Meyerson, E.A., Gasse, F., van Kreveld, S., Holmgren, K., Lee-Thorp, J., Rosqvist, G., Rack, F., Staubwasser, M., Schneider, R.R., Steig, E.J., 2004. Holocene climate variability. Quat. Res. 62(3), 243-255.

Morrill, C., LeGrande, A.N., Renssen, H., Bakker, P., Otto-Bliesner, B.L., 2013. Model sensitivity to North Atlantic freshwater forcing at 8.2 ka. Clim. Past 9(2), 955-968.

Murray, A.S., Wintle, A.G., 2000. Luminescence dating of quartz using an improved single-aliquot regenerative-dose protocol. Radiat. Meas. 32(1), 57-73.

Nance, W.B., Taylor, S.R., 1976. Rare earth element patterns and crustal evolution—I. Australian post-Archean sedimentary rocks. Geochim. Cosmochim. Acta 40(12), 1539-1551.

Nesbitt, H.W., Young, G.M., 1982. Early Proterozoic climates and plate motions inferred from major element chemistry of lutites. Nature 299(5885), 715-717.

Niu, D., Li, T., Zhong, Y., Liu, L., Li, B., 2024. Study on Holocene environmental evolution based on grain size end-member model: A case study of two outcrop sections in Salawusu River Basin. PLoS One, 19(9), e0305282.

Paterson, G.A., Heslop, D., 2015. New methods for unmixing sediment grain size data. Geochem. Geophys. Geosyst. 16(12), 4494-4506.

Prescott, J.R., Fox, P.J., Robertson, G.B., Hutton, J.T., 1994. Three-dimensional spectral studies of the bleaching of the thermoluminescence of feldspars. Radiat. Meas. 23(2), 367-375.

Prins, M.A., Weltje, G.J., Harbaugh, J.W., Watney, W.L., Rankey, E.C., Slingerland, R., Goldstein, R.H., Franseen, E.K., 1999. End-Member Modeling of Siliciclastic Grain-Size Distributions: The Late Quaternary Record of Eolian and Fluvial Sediment Supply to the Arabian Sea and its Paleoclimatic Significance, Numerical Experiments in Stratigraphy: Recent Advances in Stratigraphic and Sedimentologic Computer Simulations. SEPM Society for Sedimentary Geology.

Pye, K., 2015. Aeolian Dust and Dust Deposits. Elsevier.

Qiu, X., Cao, G., Zhang, Z., Zhao, M., He, Q., Cheng, M., Gao, S., 2022. Vertical distribution characteristics of soil organic carbon and total nitrogen density in alpine farmland and their relationships with altitude. Chin. J. Soil Sci. 53(3), 623-630 (in Chinese with English abstract).

Roberts, N., Jones, M.D., Benkaddour, A., Eastwood, W.J., Filippi, M.L., Frogley, M.R., Lamb, H.F., Leng, M.J., Reed, J.M., Stein, M., Stevens, L., Valero-Garcés, B., Zanchetta, G., 2008. Stable isotope records of Late Quaternary climate and hydrology from Mediterranean lakes: the ISOMED synthesis. Quat. Sci. Rev. 27(25), 2426-2441.

Schmidt, M.W.I., Torn, M.S., Abiven, S., Dittmar, T., Guggenberger, G., Janssens, I.A., Kleber, M., Kogel-Knabner, I., Lehmann, J., Manning, D.A.C., Nannipieri, P., Rasse, D.P., Weiner, S., Trumbore, S.E., 2011. Persistence of soil organic matter as an ecosystem property. Nature 478(7367), 49-56.

Sheldon, N.D., Tabor, N.J., 2009. Quantitative paleoenvironmental and paleoclimatic reconstruction using paleosols. Earth Sci. Rev. 95(1), 1-52.

Shi, Y., Yang, F., Long, H., Rossiter, D.G., Zhang, A., Zhang, G., 2024. Provenance of soil parent materials in relation to regional environmental changes in the Songnen Plain, Northeast China. Geoderma Reg. 38, e00848.

Song, Y., Chi, Y., Xie, Y., Kang, C., Wei, Z., Wu, P., Sun, L., Liu, R., 2023. Comparative analysis of grain size end member of Harbin loess and climatic significance. Prog. Geogr. 42(9), 1825-1840 (in Chinese with English abstract).

Song, Y.H., Herzschuh, K., Dai, H.M., Xu, J., Zhang, Z.H., Liang, S., 2022. Palynological assemblages of typical black soil profile in the eastern Songliao Plain and their age and its implication for paleoclimatic. Geol. Bull. China 41(9), 1528-1538 (in Chinese with English abstract).

Sun, D., Chen, F., Bloemendal, J., Su, R., 2003. Seasonal variability of modern dust over the Loess Plateau of China. J. Geophys. Res.: Atmos. 108(D21).

Sun, J., 2002. Provenance of loess material and formation of loess deposits on the Chinese Loess Plateau. Earth Planet. Sci. Lett. 203(3), 845-859.

Taylor, S.R., McLennan, S.M., 1985. The Continental Crust: Its Composition and Evolution. Blackwell Scientific Publications, Oxford.

Tong, Y., Angelini, M.E., Yigini, Y., Luotto, I., 2024. Global black soil distribution. Front. Agric. Sci. Eng. 11(2), 271-281.

Tsoar, H., Pye, K., 1987. Dust transport and the question of desert loess formation. Sedimentology 34(1), 139-153.

Vandenberghe, J., 1993. Changing fluvial processes under changing periglacial conditions. Z.

Geomorphol., 17-28.

Wang, Y., Cheng, H., Edwards, R.L., Kong, X., Shao, X., Chen, S., Wu, J., Jiang, X., Wang, X., An, Z., 2008. Millennial- and orbital-scale changes in the East Asian monsoon over the past 224,000 years. Nature 451(7182), 1090-1093.

Weiss, H., 2016. Global megadrought, societal collapse and resilience at 4.2-3.9 ka BP across the Mediterranean and west Asia. Pages Magazine 24(2), 62-63.

Weltje, G.J., 1997. End-member modeling of compositional data: Numerical-statistical algorithms for solving the explicit mixing problem. Math. Geol. 29(4), 503-549.

Weltje, G.J., Prins, M.A., 2003. Muddled or mixed? Inferring palaeoclimate from size distributions of deep-sea clastics. Sediment. Geol. 162(1), 39-62.

Wu, P., Xie, Y., Li, Y., Kang, C., Chi, Y., Sun, L., Wei, Z., 2022. Decoupling between circulation pattern and dust path since the last glacial in the Songnen Plain, NE China: Insights from quantitative provenance reconstruction of the Harbin dust sediments. Aeolian Res. 57, 100818.

Wu, P., Xie, Y., Li, Y., Kang, C., Chi, Y., Sun, L., Wei, Z., 2023. Provenance variations of the loess deposits in the East Asian monsoon boundary zone, Northeast China: Response to the variations of climate and wind regimes. Catena 222, 106804.

Xie, Y., Kang, C., Chi, Y., Du, H., Wang, J., Sun, L., 2019. The loess deposits in Northeast China: The linkage of loess accumulation and geomorphic-climatic features at the easternmost edge of the Eurasian loess belt. J. Asian Earth Sci. 181, 103914.

Xu, K., Dai, H., Zhang, X., Chen, C., Liu, K., Du, G., Qian, C. 2025. Black soil layer thickness prediction and soil erosion risk assessment in a small watershed in Northeast China. PLoS One, 20(6), e0324368.

Yang, F., Long, H., Gong, K., Shi, Y., Zhang, J., Zhang, A., Yang, N., Cheng, P., Pan, X., Zhang, G., 2023. Onset time and accretionary formation of Mollisols in Northeast China. Sci. Bull. 68(18), 1999-2002.

Zhang, A., Long, H., Yang, F., Zhang, J., Peng, J., Shi, Y., Zhang, G., 2024a. Reconstructing Mollisol Formation Processes Through Quantified Pedoturbation. Geophys. Res. Lett. 51(11), e2024GL108189.

Zhang, G., Long, H., Yang, F., 2023. Understanding the formation time of black soils. The Innovation Geoscience 1(1), 100010.

Zhang, S., Yang, S., Xiong, S., Guo, L., Wang, Y., Huang, X., Sun, M., Ding, Z., 2024b. Origin and depositional background of the Holocene black soil in Northeast China: Evidence from grain-size analysis and optically stimulated luminescence dating. Catena 239, 107963.

Zhang, X., Zhou, Q., Chen, W., Wang, Y., Tong, D.Q., 2015. Observation and modeling of black soil wind-blown erosion from cropland in Northeastern China. Aeolian Res. 19, 153-162.

Zhao, H., Yanchou, L., Yin, J., 2007. Optical dating of Holocene sand dune activities in the Horqin sand-fields in inner Mongolia, China, using the SAR protocol. Quat. Geochronol. 2(1), 29-33.